Macromolecules

ARTICLE

pubs.acs.org/Macromolecules

Drastic Control of Texture in a High Performance n-Type Polymeric Semiconductor and Implications for Charge Transport

Jonathan Rivnay,[†] Robert Steyrleuthner,[‡] Leslie H. Jimison,[†] Alberto Casadei,[§] Zhihua Chen,[∥] Michael F. Toney,[⊥] Antonio Facchetti,[∥] Dieter Neher,[‡] and Alberto Salleo*[,†]

[†]Materials Science and Engineering, Stanford University, Stanford, California 94305, United States

[‡]Institute of Physics and Astronomy, University of Potsdam, Potsdam-Golm, Germany

[§]Department of Physics, University of Bologna, Bologna, Italy

[∥]Polyera Corporation, Skokie, Illinois 60077, United States

[⊥]Stanford Synchrotron Radiation Lightsource, Menlo Park, California 94025, United States

Supporting Information

ABSTRACT: Control of crystallographic texture from mostly face-on to edge-on is observed for the film morphology of the n-type semicrystalline polymer {[*N*,*N*-9-bis(2-octyldodecyl)naphthalene-1,4,5,8-bis(dicarboximide)-2,6-diyl]-*alt*-5,59-(2,29-bithiophene)}, P(NDI2OD-T2), when annealing the film to the polymer melting point followed by slow cooling to ambient temperature. A variety of X-ray diffraction analyses, including pole figure construction and Fourier transform peak shape deconvolution, are employed to quantify the texture change, relative degree of crystallinity and lattice order. We find that annealing the polymer film to the melt leads to a shift from 77.5% face-on to 94.6% edge-on lamellar texture as well as to a 2-fold increase in crystallinity and a 40% decrease in intracrystallite cumulative disorder. The texture change results in a significant drop in the electron-only diode current density through the film thickness upon melt annealing, while little change is observed in the in-plane transport of bottom gated thin film transistors. This suggests that the texture change is prevalent in the film interior and that either the (bottom) surface structure is different from the interior structure or the intracrystalline order and texture play a secondary role in transistor transport for this material.

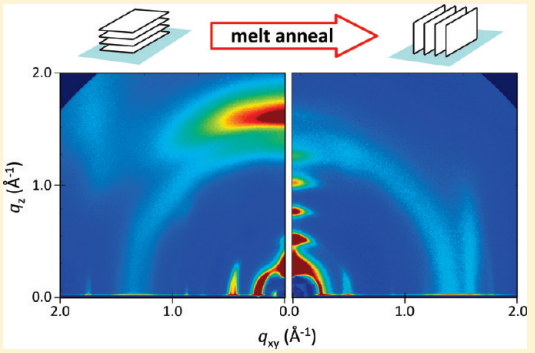

INTRODUCTION

High performing semiconducting polymers have generated significant interest due to their potential commercialization in low-cost logic circuits, organic light-emitting diodes, solar cells, and sensors.[1,2] These polymers are readily solution processable, are compatible with flexible substrates, increasingly show air-stable operation, and consistently exhibit thin film transistor (TFT) mobilities >0.1 cm^2/(V s). While high performing hole-transporting or p-type polymeric semiconductors have been readily studied for over a decade, only recently have electron transporting (n-type) polymers shown high mobilities. The combination of n-type and p-type polymeric materials is important for all-polymer photovoltaics[3,4] and complementary logic circuit applications.[5,6] One such n-type polymer, poly{[*N*,*N*-9-bis(2-octyldodecyl)naphthalene-1,4,5,8-bis(dicarboximide)-2,6-diyl]-*alt*-5,59-(2,29-bithiophene)}, P(NDI2OD-T2), has shown electron mobility consistently >0.1 cm^2/(V s) and up to 0.85 cm^2/(V s) in a staggered top gate transistor geometry; reported diode mobilities are >3 × 10^{-3} cm^2/(V s).[7−9] However, to better understand and improve the performance in this unique polymer family, in-depth structure−property relations must be established.

The p-type polymeric semiconductors benefit from a wealth of structure−property knowledge and related rational design. For instance, it has been shown that molecular weight, solvent choice, spin-casting conditions, and surface treatments can cause variations in the microstructure, texture, and packing of poly(3-hexylthiophene), P3HT, and therefore change the mobility by 5 orders of magnitude.[10−13] As a result of the knowledge gained from these film forming studies and from the structure of P3HT, high-performance polythiophene derivatives such as PBTTT [poly(2,5-bis(3-tetradecylthiophen-2-yl)thieno[3,2]thiophene)] were developed. With a lower density of side chains and a more rigid conjugated core, this polymer displays side-chain interdigitation and highly textured lamellar packing with mobilities now reported >1 cm^2/(V s).[14−18] While such investigations within a well-studied system of materials (polythiophenes) have led to quite astonishing improvements in performance, new classes of

Received: April 14, 2011
Revised: May 12, 2011
Published: June 09, 2011

materials pose new challenges and bring into question seemingly well-established design rules.

The high electron mobility of P(NDI2OD-T2) in both the transistor and single carrier device configuration (parallel and perpendicular to the substrate plane, respectively) is unprecedented for polymers and is therefore of interest because it implies great potential in multiple device applications. Moreover, this unusual property is of general interest as it suggests that something about the ordering or morphology of this molecule aids or allows for intrinsically high performance in both the in-plane and out-of-plane directions. While much information was initially reported with respect to TFT performance, stability, and chemistry,[8] structurally, there is limited reported information about this material. Recent diffraction experiments revealed that P(NDI2OD-T2) packs in a lamellar fashion, but under the spin-casting conditions and solvents used for the fabrication of high performing transistors, significant lamellar diffracted intensity was observed in plane.[19] The relevant lattice spacings were determined from grazing incidence X-ray diffraction. Interestingly, the crystalline texture was largely in the face-on configuration, with the conjugated core lying nearly flat or parallel to the substrate and lamellar stacked planes ordered in-plane. Consequently, the π-stacking direction was out-of-plane. Given what is known about the polythiophene family, where edge-on or out-of-plane lamellar stacking implies 2D charge transport in the $\pi-\pi$ stacking and chain backbone directions in the substrate plane—which is often thought to be a requirement for obtaining high-performance semicrystalline polymer transistors—it is surprising that face-on packing could yield such high TFT mobilities. Therefore, some other mechanism dominates or overcomes this inherent microstructural disadvantage, and it was suggested that extensive intergrain connectivity strongly aids TFT transport.[19] The bulk out-of-plane π-stacking, however, explained quite well the high electron-only device and time-of-flight mobilities observed by Steyrleuthner et al.[9] Interestingly, high-mobility p-type semiconducting polymers exhibiting mostly face-on texture have also been recently reported, again, with limited structural information.[20]

Recently, the structure of P(NDI2OD-T2) has been investigated using near-edge X-ray absorption fine structure (NEXAFS) spectroscopy and surface sensitive (small angle of incidence) grazing incidence X-ray diffraction (GIXD), due to the relevance of near-surface structure to the performance of top-gated TFTs.[21] While the same general crystalline structure was found for the bulk and near the top of the film, the NEXAFS spectra suggested that there is little tendency for core or side chain ordering either in or out of the substrate plane. This result was interpreted by the authors as suggesting a large amorphous fraction of the polymer near the top surface. A series of heating experiments were performed, including melt-quenching into a highly disordered, amorphous state.[21] Top-gated TFT performance began to suffer once the annealing temperature exceeded ~200 °C. From their interpretation of a large amorphous content, the authors suggested that the observed high performance cannot be due to the crystalline component of the films.

These studies serve as a basis to further investigate the effects of semicrystalline ordering and texture on device performance in P(NDI2OD-T2). It is important that the origin of the high performance for rylene−thiophene polymers be thoroughly understood, since this can lead to improvements in the performance in this unique polymer family. Controlling the semicrystalline film texture of these materials serves as a tool both to better understand their intrinsic performance and to tune their film properties for different device applications.

In this work we explore the effect of heat treatment and melt annealing on the texture, relative crystallinity, and crystalline lattice disorder. Furthermore, we relate these microstructural quantities to the electrical properties of P(NDI2OD-T2) in both bottom-gate transistor and sandwich device geometries. Specifically, we focus on films annealed between 150 and 180 °C and those annealed above the melting point (300−320 °C). We find that heating P(NDI2OD-T2) above its melting point and slowly cooling the film induces a drastic texture change from a mixed, largely face-on packing, which has been previously reported,[19] to a pronounced edge-on packing. We are able to quantify the relative crystallinity of the lamellar packing and crystallite orientation distribution using pole figures and the change in crystalline lattice disorder using Fourier transform peak shape analyses. We also investigate this texture transition using in-situ grazing incidence X-ray scattering. The texture change is found to have little effect on bottom-gate thin film transistor mobility (~0.1 $cm^2/(V\ s)$ for both textures) but a marked effect on the diode current (decreased current by ~6 times). This unprecedented texture control suggests that transport along the substrate normal can be tuned but that the crystalline texture found in the bulk does not necessarily affect bottom-gate TFT performance.

EXPERIMENTAL METHODS

Materials. Poly{[*N*,*N* 9-bis(2-octyldodecyl)naphthalene-1,4,5,8} (P(NDI2OD-T2), Polyera ActivInk N2200) was used as received (Polyera Corp, Skokie, IL). Synthesis and purification are described elsewhere.[7,8] The average polymer molecular weight is 300 kDa, with a polydispersity index (PDI) of ~4. Silicon wafers were purchased from Silicon Quest International, Santa Clara, CA, and were cleaned by successive sonication in acetone, methanol, and isopropanol before UV-ozone treatment. PEDOT:PSS was obtained from H.C. Starck GmbH, Germany, under the trade name Clevios P VP AI4083. Indium tin oxide (ITO)-covered glass was obtained from Präzisions Glas & Optik GmbH, Germany, and cleaned by ultrasonication in acetone, detergent solution, deionized water, and isopropanol. These substrates have a 25 nm thick SiO_2 protection layer between the soda-lime glass and the conducting ITO of 100 nm thickness and 15 Ω/□ sheet resistance.

Film Fabrication. Films used for XRD were spun on silicon with native oxide; those for TFTs and diodes were prepared as described below. XRD and TFT substrates were treated with an octadecyltrichlorosilane (OTS) self-assembled monolayer after a 20 min UV-ozone treatment. Film preparation was done in a N_2 glovebox (<5 ppm of O_2). For XRD and TFT samples, films were spun-cast from a 1,2-dichlorobenzene (DCB) solution (5−10 mg/mL) at 1000−1200 rpm for 60−90 s, yielding films of 60−70 nm thickness (determined by AFM). Samples denoted "as-prepared" were unannealed, those denoted "annealed" were annealed at 150−180 °C for 30 min, and those called "melt-annealed" were annealed at 300−320 °C for 30−40 min and then cooled slowly at an overall rate of 5−10 °C/min. It has been shown that annealing to these high temperatures does not cause degradation of the polymer films.[21]

X-ray Characterization. X-ray scattering was performed at the Stanford Synchrotron Radiation Lightsource (SSRL) on beamline 7-2 (high-resolution grazing incidence), 2-1 (high-resolution specular scan with a point detector), and 11-3 (2D scattering with an area detector, MAR345 image plate, at grazing incidence). The incident energy was 8 keV for beamlines 7-2 and 2-1 and 12.7 keV for beamline 11-3. The diffracted beam was collimated with 1 mrad Soller slits for high-resolution in-plane scattering and with two 1 mm slits for specular diffraction. For

both grazing incidence experiments, the incidence angle was slightly larger than the critical angle, ensuring that we sampled the full film depth. Scattering data are expressed as a function of the scattering vector $q = 4\pi/\lambda \sin\theta$, where θ is half the scattering angle and λ is the wavelength of the incident radiation. Here, q_{xy} (q_z) is the component of the scattering vector parallel (perpendicular) to the substrate. All X-ray scattering measurements were performed under a He atmosphere to reduce air scattering and beam damage to the sample. In-situ heating experiments at beamline 11-3 were carried out using a custom built chamber and heating stage which has been described previously.[22] Measurements were performed at the indicated temperatures where patterns were collected after allowing for a 5 min equilibration time after the target temperature was reached. In-situ scans lasted 5−10 min. An uncertainty of ±3 °C in the temperature is due to variations in the surface temperature of the sample holder along the beam path as well as differences in the surface temperature relative to the thermocouple. All initial 2D GIXS data processing and analysis was done with the software package WxDiff.[23] The data were distortion-corrected (θ-dependent image distortion introduced by planar detector surface) before performing quantitative analysis on the images.

Pole figures of the P(NDI2OD-T2) films were measured using a method described previously.[24] Briefly, for each pole figure, intensity data from a two-dimensional grazing incidence diffraction pattern and a two-dimensional local specular pattern are stitched together to accurately describe diffracted intensity of a certain Bragg reflection, in this case the (100), as a function of χ (where χ is defined as the angle between the crystallite orientation and the surface normal). Here, we proceed one step beyond that reported in Baker et al.[24] and collect intensity within 2° of the surface normal by collecting high-resolution rocking data of the (100) reflection with a point detector,[25] stitching this into the final pole figure. This procedure not only provides higher resolution data near $\chi = 0$, but the quantitative intensity associated with a defined beam footprint allows for accurate normalization between samples (after normalization by sample thickness). Since the films investigated in this study are fiber-textured (possessing an isotropic crystalline structure in the plane of the substrate), the one-dimensional pole figures shown herein are accurate representations of all the diffracting material. A resolution-limited peak corresponding to a significant population of crystallites oriented with their (100) repeat vector lying within ~0.03° of the surface normal (perfectly oriented crystallites) is observed.[25] The integrated intensity from χ = 0° to χ = 90°, calculated according to eq 3, is directly proportional to the degree of crystallinity, where degree of crystallinity is defined as the volume fraction of crystalline material in the film.[26]

$$\mathrm{DoC} \propto \frac{\Delta\beta\Delta\theta}{2\pi}[I_{\mathrm{peak}} - I_{\mathrm{baseline}}] + \int_0^{\pi/2} \sin(\chi) I(\chi)\, \mathrm{d}\chi \qquad (1)$$

In the preceding equation, the slowly varying intensity is integrated separately from the resolution limited peak, if it is present, which is resolution-limited due to details of the beamline. The first term of the right-hand side of eq 1 refers to the integration of the resolution-limited peak where $\Delta\beta$ is the horizontal (out-of-scattering plane) acceptance angle and $\Delta\theta$ is the vertical (in the scattering plane) resolution (acceptance). I_{peak} and I_{baseline} are defined as the maximum and minimum intensity of the resolution limited peak, respectively. The pole figures can be used to quantitatively compare the relative degree of crystallinity between different samples—a value of 1 is given to the most crystalline film in the data set, against which other films are compared; note that this is not absolute crystallinity. Moreover, calculating the integrated pole figure intensity along confined angular ranges allows for the comparison of film texture in a quantitative fashion.

Warren−Averbach Fourier transform data analysis was utilized to determine the average column length (related to crystallite size) and cumulative disorder of the crystalline regions of P(NDI2OD-T2) films. The basic analysis routine has been described previously,[27,28,21] and a more in-depth description of the specific methodology and error propagation routine employed is found in refs 29 and 30. Briefly, two main sources of broadening are treated: a diffraction-order-independent component that reflects the size of the crystallites and an order-dependent portion that is affected by paracrystalline disorder as well as variations in the average lattice spacing.[27] Paracrystalline disorder is described as a statistical fluctuation of local lattice spacings.[31,32] In this model, each diffraction peak is constructed from the superposition of waves scattered by units whose distortions from the ideal lattice are described by Gaussian statistics and belong to columns of unit cells along the [hkl] direction. The normalized nth coefficient of the Fourier transform of the mth-order diffraction peak is then given by

$$A_m(n) = A^s_m(n) \exp[-2\pi^2 m^2 (ng^2 + n^2 e_{\mathrm{rms}}{}^2)] \qquad (2)$$

where $A^s{}_m(n)$ is the size-related broadening contribution which depends on the column length distribution in the sample, g is the paracrystalline disorder, and e_{rms} is the lattice parameter fluctuation reduced variance.[33] In this case we assume a single column length, M, since this is simple and provides sufficiently accurate determination of g and e_{rms}. The column length is loosely akin to a grain size in the crystallographic direction under consideration (along [hkl]). The collected data are corrected for beam footprint, the background is subtracted, and the relevant peaks are isolated from other peaks through a peak fitting deconvolution. A Fourier transform of the isolated peaks is followed by a normalization step after which a full fit to eq 2 is performed, weighted to the variance of the propagated error. The extracted parameters in this case are an average column length, M, and the parameters for cumulative disorder, g and e_{rms}, described above.

Microscopy. Optical microscopy was performed on temperature-treated film on glass with an Olympus BX51 polarized light microscope. Atomic force microscopy (AFM) data were collected using a NT-MDT "Solver" instrument in tapping mode.

Transistor Fabrication and Testing. Films for device characterization were spun on Si wafers coated with 200 nm thermal SiO_2 gate dielectric layer (C_d = 17nF). After substrate cleaning and OTS treatment, the P(NDI2OD-T2) active layer were spun-cast as detailed above. Au source and drain electrodes were vapor deposited through a shadow mask, defining channels with length (L) of 200 μm and widths (W) in the 0.5−1 mm range. All TFT testing was performed under vacuum. Variable temperature data were tested and mobility extracted in the linear regime (V_d = 10 V); linear and saturation mobilities were both extracted at room temperature, under vacuum, using the following equations:[34,35]

$$\begin{aligned} I_{\mathrm{d,lin}} &= \frac{W}{L}\mu C_{\mathrm{d}}(V_{\mathrm{g}} - V_{\mathrm{t}})V_{\mathrm{d}} \\ I_{\mathrm{d,sat}} &= \frac{W}{2L}\mu C_{\mathrm{d}}(V_{\mathrm{g}} - V_{\mathrm{t}})^2 \end{aligned} \qquad (3)$$

where μ is the mobility, C_d is the capacitance per unit area, V_g is the gate voltage, and V_t is the threshold voltage.

Electron-Only Device Fabrication and Testing. Electron-only devices based on P(NDI2OD-T2) were fabricated following the approach published in ref 36. The PEDOT:PSS on top of glass acts as a smoothing layer for the bottom aluminum electrode. It has been shown that the use of flat bottom electrodes largely reduces negative differential resistance (NDR) effects, which would inhibit the reliable analysis of electron currents. P(NDI2OD-T2) was dissolved in chlorobenzene at a concentration of 30 mg/mL. Spin-coating of this solution yielded macroscopically homogeneous layers with thicknesses of 310 ± 10 nm (measured using a Dektak 3ST profilometer in air). Samarium was used as the electron injecting top electrode, as it was shown to yield the highest injection efficiency compared to other low work function materials.[9] All metal contacts were fabricated by thermal evaporation at a

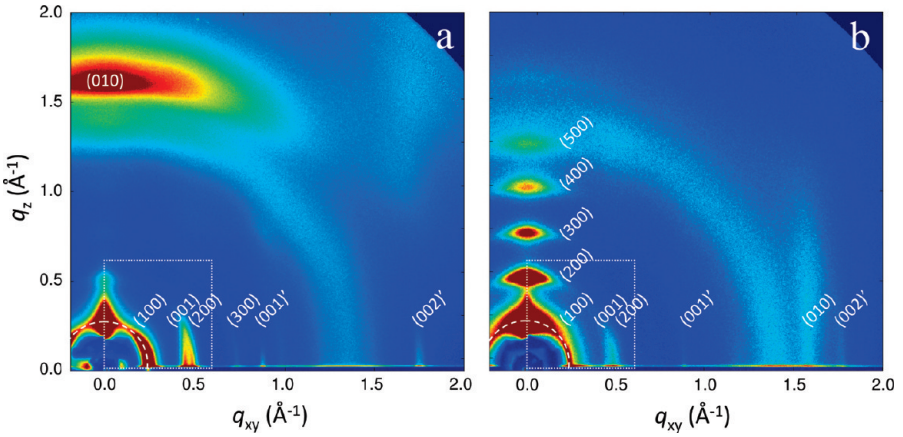

Figure 1. 2D grazing incidence X-ray scattering patterns of P(NDI2OD-T2) before (a) and after (b) annealing to the melt and slowly cooling the sample. The dotted boxes show the region displayed in the in-situ temperature series shown in Figure 3, while the dashed arc qualitatively represents the cut along which pole figures are measured (Figure 2c).

base pressure <2 × 10^{-6} mbar. The metals used had a purity of 99.99%. The evaporator vacuum chamber is directly connected to a nitrogen-filled glovebox system, allowing the loading of evaporation crucibles under an inert atmosphere.

Current−voltage characteristics were measured inside a glovebox by a computer-controlled Keithley 2400 source/measure unit with the Sm top electrode biased negatively. Oxygen and water contaminations of the glovebox atmosphere were <2 ppm for this device preparation, and samples were transferred without contact to air. Temperature treatment of the semiconducting layer was carried out before deposition of the Sm top contact. To check whether the bottom aluminum electrode (or the PEDOT:PSS layer) is affected by the high temperature treatment (e.g., through oxidation or degradation), we also fabricated sandwich electron-only devices with only ITO bottom contacts. This resulted in a strong increase in NDR effects at low voltages.[36] However, these devices exhibited comparable current densities at higher fields (when compared to devices with a PEDOT:PSS/Al contact that underwent the same thermal annealing), confirming no measurable effect of the thermal treatment on the aluminum bottom contact.

RESULTS AND DISCUSSION

In the following section, we discuss the changes in P(NDI2OD-T2) film microstructure and morphology with a simple procedure of annealing the films to the melt and slowly cooling back to room temperature. We first describe the observed changes in texture and crystalline packing using X-ray diffraction and then discuss the morphological changes using AFM and optical microscopy. Finally, we address the implications of the observed structural changes on charge transport in P(NDI2OD-T2) devices.

Observation and Control of Crystalline Texture. X-ray diffraction serves as a powerful tool to investigate the crystalline structural properties of films as it allows one to obtain general packing motif and details of intragrain disorder and film texture. Comparing the diffraction profiles of annealed (150 °C) and melt-annealed films (Figure 1) reveals a large texture change from largely face-on (as previously reported)[19] to an edge-on character. The latter is commonly observed for semicrystalline polymers, especially those in the polythiophene family.[11] We begin by first investigating the diffracted intensity in the directions parallel and perpendicular to the film plane. The specular geometry, associated with crystalline planes parallel to the substrate, stacked in the out-of-plane direction, is represented to first order as a cut along the y-axis ($q_{xy} \approx 0$) in the 2D-GIXS shown in Figure 1. The grazing exit angle geometry, on the other hand, represents the in-plane diffraction along the horizon of the diffraction patterns ($q_z \approx 0$).

When annealing at 150 °C, a broad peak associated with the π-stacking repeat (q = 1.6 Å^{-1}) is observed in the nominally specular direction, with intense lamella stacking, (h00), peaks evident in-plane. Four orders of these lamellar peaks (those from planes separated by the branched alkyl chains) are observed in-plane along with a number of peaks due to the chain backbone repeat, as previously reported.[19] After annealing the films to the melt (as determined by in-situ diffraction observations) for 40 min and cooling to room temperature, the lamellar repeats appear highly textured out of plane and more intense: five diffraction orders are observed in the nominally specular direction. Meanwhile, the π-stacking diffraction reappears, but now in-plane. These measurements show that upon melting and resolidification the polymer chains switch from a face-on packing to edge-on packing, with the chain backbone and π-stacking direction in the plane of the substrate. This general finding is confirmed with high-resolution X-ray diffraction (Figure 2), from which accurate peak positions and widths can be extracted (Supporting Information Table S1). Additionally, it is observed that the average lamellar d-spacing contracts slightly from d_{100} = 25.03 Å for the majority (in-plane) crystallites before melting to d_{100} = 24.35 Å for the majority (out-of-plane) crystallites after melt-annealing.

The texture change can be monitored in-situ using grazing incidence diffraction with a 2D detector. During the annealing process it is clear that the majority lamellar crystallite population (face-on) persists, until the melt is reached after which the edge-on crystallites dominate on cooling. This behavior has previously been observed in-situ for films of P3HT and P3HT blends spun from a low boiling point solvent and annealed above the melting temperature.[22] The texture reorganization is observed by monitoring the (100) peak intensity in the nominally specular geometry and the grazing geometry (Figure 3a). As the 150 °C annealed sample is heated, the peak intensity of both face-on and edge-on lamellar crystallites increases, with the face-on texture dominating. At a temperature between 225 and 250 °C, the intensities of reflections from both the face-on and edge-on crystallite populations start to diminish until the melt is reached, when they disappear. Upon

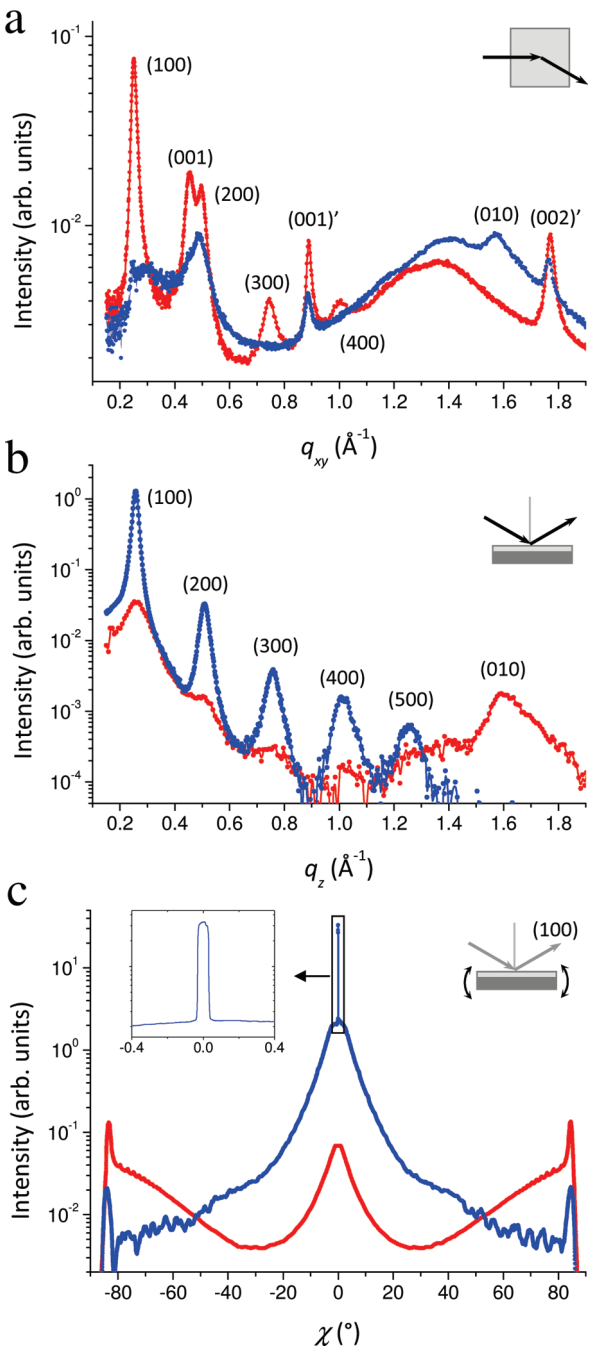

Figure 2. High-resolution grazing incidence (a) and specular (b) X-ray diffraction scans of P(NDI2OD-T2) films annealed at 150 °C (red) and melt-annealed (306 °C) and slow cooled (blue). Complete pole figures (c) of the (100), lamellar-stacking peak, quantitatively illustrating film texture (inset: high-resolution rocking curve from the melt-annealed sample). The melt-annealed film shows a significantly higher fraction of edge-on crystallites and is more crystalline than before melt-annealing.

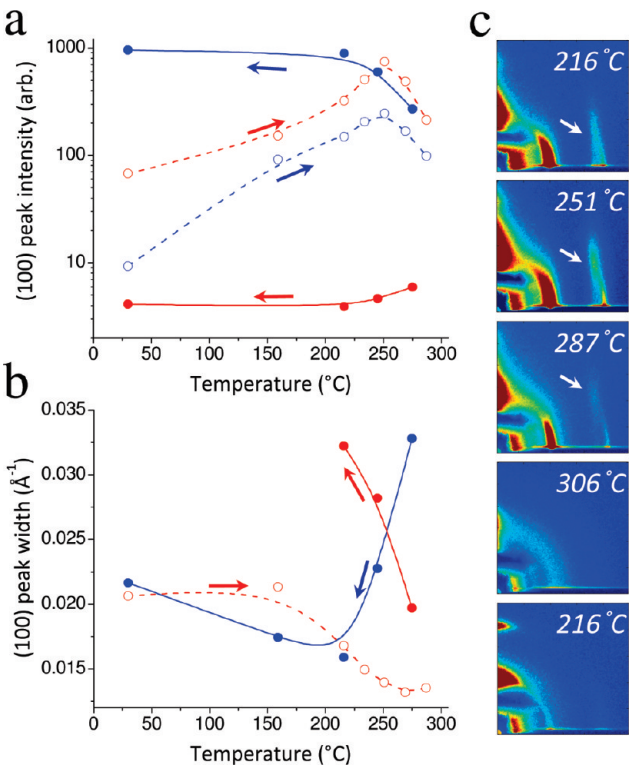

Figure 3. In-situ grazing incidence X-ray diffraction during the melt anneal process: the (100) peak intensity (a) and peak width (b) of the lamellar stacked population. Red is the in-plane (100) peak, and blue is the out-of-plane (100) peak. Dotted lines and open symbols represent the peak upon heating; solid lines and closed symbols are upon cooling from the melt. All values are taken from 2D GIXS cuts. The close-up 2D GIXS patterns (c) of melt-annealed films are shown for the range above 200 °C, where the change in texture is clearly evident in the (100) and the (001) peak; white arrows show a gradual transition of the (001) peak to higher q_z values at the temperature range between 215 and 290 °C. The 2D GIXS patterns here are from 0 to 0.6 Å^{-1} in q_{xy} and q_z; the scale and position of the 2D GIXS patterns shown here with respect to the entire pattern are represented in Figure 1 as a dotted region.

cooling slowly from the melt, a large textural change is observed as an almost immediate increase in the edge-on population, accompanied by a drop in the face-on peak intensity. The peak intensities plateau below ~200 °C.

Accompanying the information obtained from monitoring peak intensity, it is also informative to examine the respective peak widths (Figure 3b). Measurement of edge-on peak widths on heating is hindered due to the low q_z value of the (100), the large peak breadth (~0.09 Å^{-1} at room temperature measured with a high-resolution point detector), and convolution with both high background reflectivity scattering and beam stop shadowing. Slight discrepancies in peak position and width compared to the high-resolution data in Supporting Information Table S1 may be due to the low resolution and distortions associated with the flat 2D detector. Nevertheless, we are able to monitor the in-plane (100) peak breadth and observe a small drop at $T \sim 200-250$ °C—a result indicative of either growth in the crystalline coherence length or an increase in intracrystalline ordering by, perhaps, expulsion of defects. On cooling from the melt, the peak width of the now minority face-on crystallites increases to the point where their width cannot be confidently extracted from the background. Together with the information on peak intensity, this suggests that the face-on crystallites are now significantly fewer in number, quite small, and/or highly defective. These findings also suggest that the majority edge-on crystallite population grow from the melt.

A drop in TFT mobility has been previously noted for top-gated devices annealed above 200 °C.[21] Our data suggest that a

Table 1. Results from Quantitative Complete Pole Figure and Warren−Averbach Full Fit Peak Shape Analyses

sample	annealed, 150 °C	melt-annealed, 306 °C
$d_{100,majority}$ (nm)	2.50	2.44
r.DoC	0.56	1
% contributions of χ range		
0°−30° (edge on)	22.5	94.6
30°−90° (face on)	77.5	5.4
WA analysis, majority		
M (nm)	35 ± 13[a]	27.4 ± 1.5
g (%)	6.1 ± 0.9	3.8 ± 0.2
e_{rms} (%)	2.2 ± 1.0	1.9 ± 0.3

[a] The high error values found for the analysis of 150 °C annealed sample are due to a combination of larger error values in the raw data and convolution of the second diffraction order peak, (200).[29]

morphological change in the packing could contribute to the decreased performance. In addition to changes observed in the (100) diffraction peak intensity and width above, we also note that there is a qualitative change in the scattering pattern associated with the chain backbone, (001) peak, in the 200−250 °C temperature regime (Figure 3c). Specifically, there is a shift in the (001) peak position to higher q_z values, while the in-plane scattering vector, q_{xy}, remains unchanged. This can be interpreted as a subtle molecular rearrangement with a slight change in unit cell parameters; this effect could be caused, for example, by a deviation in the out-of-plane unit cell angles due to a change in tilt of the chain backbone. This conclusion is supported by a decreased (100) d-spacing (not shown) in this same temperature range. Additionally, although the diffracted signal is weak, we do not see this shift in the (001)′ and (002)′ peak (the in-plane peaks attributed to chain backbone ordering in another polymorph), further supporting the possibility that there are two phases present.[19] Although this set of data points to some changes in the molecular arrangement/unit cell, the mechanism causing this observed change is unknown. Possibilities include rearrangement of the branched side chains or complications in thermal transition analysis due to the large polydispersity index (≈4) of this polymer film.

Quantification of Texture Change and Relative Crystallinity. While the collection of in-situ data supports the finding of considerable texture change on melt-annealing, an accurate quantification of crystallite orientation and relative crystallinity can only be determined by assembling complete pole figures. Figure 2c compares pole figures of the lamellar (100) reflection for a film annealed to 150 °C and a film annealed to the melt. The film annealed to 150 °C shows a bimodal orientation distribution, with peaks in intensity near $\chi = 0°$, attributed to edge-on crystallites, and near $\chi = \pm 90°$, due to the face-on crystallites. After annealing the film to the melting point, followed by a slow cool, there is a drop in intensity near $\chi = \pm 90°$, consistent with a decrease in the population of face-on crystallites occurring at the same time as a large increase in the intensity near $\chi = 0°$, which is consistent with an increase in the edge-on population. Moreover, we observed the appearance of a resolution limited peak at $\chi = 0°$ for the melt-annealed sample. This peak is due to perfectly oriented edge-on crystallites that are nucleated directly from the buried polymer−substrate interface as previously shown in semicrystalline films of P3HT.[25] We speculate that upon spin-casting a small population of edge-on crystallites are nucleated at the dielectric interface and persist as seeds when the bulk of the film is melted. These seed nuclei template the growth of edge-on crystallites when the melt is slowly cooled. Alternatively, it is possible that the whole film is melted, and on cooling, edge-on crystallites rather than face-on crystallites grow from heterogeneous nucleation at the dielectric interface. This behavior has also been observed in the P3HT system.[22] Integrated intensities indicate that the melt annealed sample is approximately twice as crystalline as the sample annealed to 150 °C for 30 min. We can use the pole figures to quantify the percentage of edge-on and face-on crystallites, where edge-on crystallites are defined as crystallites with their lamellar-stacking direction oriented within 30° of the surface normal ($\chi = 0°$) and face-on with the lamellar direction within 30° of the in-plane direction ($\chi = 90°$). Before the melting procedure, 77.5% of crystallites are face-on, while after melting, 94.6% of the crystallites are edge-on (Table 1). Hence, the texture shift is drastic.

Quantification of Crystallite Size and Local Crystalline Lattice Disorder. To this point we have described the texture change and quantified the relative crystallinity before and after melt-annealing. In both cases we find that multiple diffraction orders of the lamellar stacking repeat (i.e., (100), (200), (300), etc.) are evident: in-plane for the 150 °C annealed films and out-of-plane for the melt-anneal films. This, again, corresponds to the majority lamellar population in both cases. Additionally, the benefit of observing multiple well-resolved diffraction orders allows for quantitative Fourier transform peak shape analysis for determining average column length (related to crystallite size), lattice parameter fluctuation, and intracrystalline static disorder. By isolating and normalizing the first three diffraction orders of both films, it is readily observed that the first-order peaks are of similar breadth (~0.02 Å^{-1}), but the (200) and (300) peaks of the 150 °C annealed film show more relative broadening than the melt-annealed film (Figure 4a,b). It is known that the progressive broadening within a family of diffraction peaks is indicative of a higher degree of cumulative disorder.[27,33] Using an error-weighted full fit analysis of the Fourier transform of the isolated peaks[29,30] (Figure 4c,d), we are able to determine these values with confidence. We find that both the average column lengths (M) are approximately the same, with the melt-annealed sample having M = 27 nm, while that of the 150 °C annealed sample is 35 nm, which is not surprising given the similar (100) peak breadths observed for both majority populations. The finding of similar column length of the majority crystallite population, regardless of face-on or edge-on packing, may indicate an intrinsic (or "natural") crystallite size in the alkyl-stacking direction of this material. It is also found that the lattice parameter fluctuation (e_{rms}), a measure of the variance in d-spacing from one crystallite to another or from one region of the film to another, is also similar for both films, decreasing from 2.2% to 1.9% upon melt-anneal. The largest change on melt annealing is the 40% drop in the paracrystalline disorder (g) from 6.1% to 3.8%, explaining the difference in peak broadening. These findings show that slow cooling from the melt has the effect of not only tuning the texture in the thin film but also improving the crystallinity and intracrystallite order. While this measure of cumulative disorder treats only one crystallographic direction, it can be an indicator of relative change in ordering within the crystallites as a whole. The degree of cumulative disorder in semicrystalline polymers has recently been shown by modeling to introduce localized tail states in the density of states, which directly affects intragrain charge transport.[30]

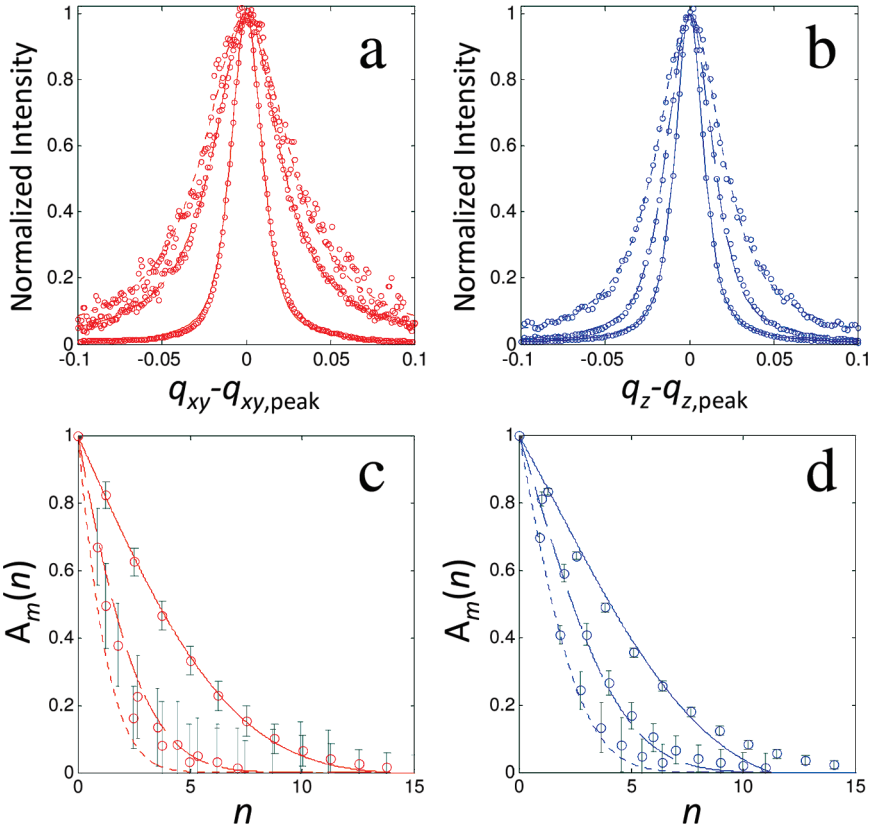

Figure 4. Warren−Averbach full-fit analysis of P(NDI2OD-T2) used to accurately determine lamellar crystallite size and lattice disorder of the majority population in annealed (red) and melt-annealed (blue) films. Isolated and normalized peaks (a, b) and their Fourier transforms (c, d) for the (100), (200), and (300) peaks (solid, dashed, and dotted, respectively). Note both films have similar (100) peak breadth, but the melt-annealed films show less peak broadening for higher diffraction orders.

Surface and Bulk Morphology Variations Probed by AFM and Optical Microscopy. Additional information on the morphology of these thin films can be gained with atomic force microscopy (Figure 5). Thermal annealing of P(NDI2OD-T2) films at up to 180 °C has no visible effect on the film topography, and the typical ribbonlike features of the as-prepared layer are well preserved, consistent with previous work.[8,21] These features have widths on the order of tens of nanometers, consistent with the column lengths extracted from X-ray characterization. Phase contrast images, which are highly sensitive to surface properties like adhesion and the mechanical stiffness, of as-prepared and 180 °C annealed films show domains in the micrometer range. Films annealed above T_m and slow cooled to room temperature have a completely different morphology. The ribbonlike structure has disappeared entirely and the surface roughness increases significantly, from ∼1.5 to ∼7 nm.

Optical polarized light microscopy of the as-prepared and 180 °C annealed films (Figure 6) reveals dichroic features on the same length scale comparable to the AFM phase images. This finding is indicative of a homogeneous orientation of P(NDI2OD-T2) chains within these domains. Melt-annealing leads to a large increase in the domain size and macroscopic alignment over a large area, suggesting that crystalline regions within these domains are well-oriented with respect to one another and thus exhibit low angle boundaries between crystallites, which has been shown to provide efficient pathways for charge transport.[37] The fact that the as-prepared films already show crystalline behavior in optical polarized light microscopy underlines the strong tendency of P(NDI2OD-T2) to stack and form domains with distinct orientation.

As a brief comparison, we also studied samples that had been heated at 320 °C followed by rapid cooling (by placing the hot sample onto a cold metal plate). The film topography of such fast cooled samples was rather featureless and optical microscopy gave no evidence for large dichroic domains. We propose that, in contrast to slow cooling, heating above the melt temperature and rapidly cooling the films results in a rather amorphous bulk morphology. This is in agreement with previous near-surface GIXD studies.[21]

Implications of Crystalline Texture Change for Charge Transport. The implications for charge transport of P(NDI2OD-T2) film microstructural changes are evident by fabricating TFTs and electron-only diodes. This study allows us to observe the electrical transport in the plane of the film, near the semiconductor−dielectric interface (for bottom-gate TFTs), as well as in the out-of-plane direction, through the thickness of the film (for electron-only devices).

We first tested device performance of bottom-gate transistors. The saturation regime mobility was extracted for these devices before and after melt-annealing of the semiconductor. Both devices attained similar on-currents and saturation mobilities of 0.14 and 0.11 $cm^2/(V\ s)$ for the 150 °C annealed and melt-anneal samples, respectively, with threshold voltages of +13 and +11 V (Figure 7a). To the best of our knowledge, these values represent the highest reported mobilities of P(NDI2OD-T2) in the bottom-gate geometry. The linear regime mobilities (V_d = 10 V)

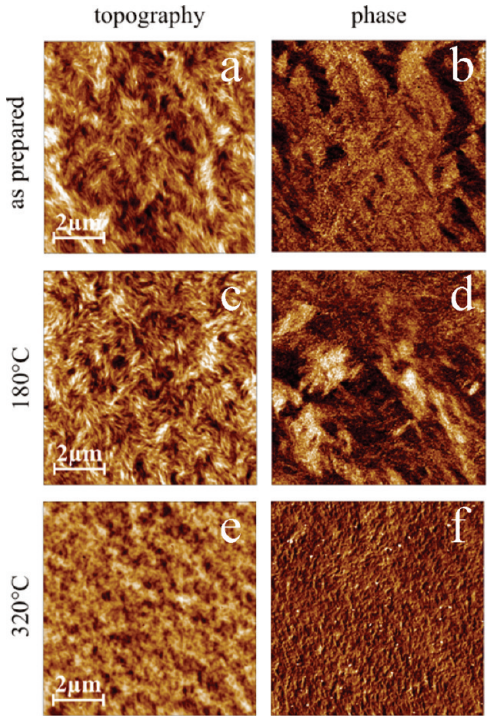

Figure 5. Atomic force microscopy (AFM) of as-prepared (a, b), annealed (c, d), and melt-annealed (e, f) P(NDI2OD-T2) films: (a, c, e) topography; (b, d, f) phase.

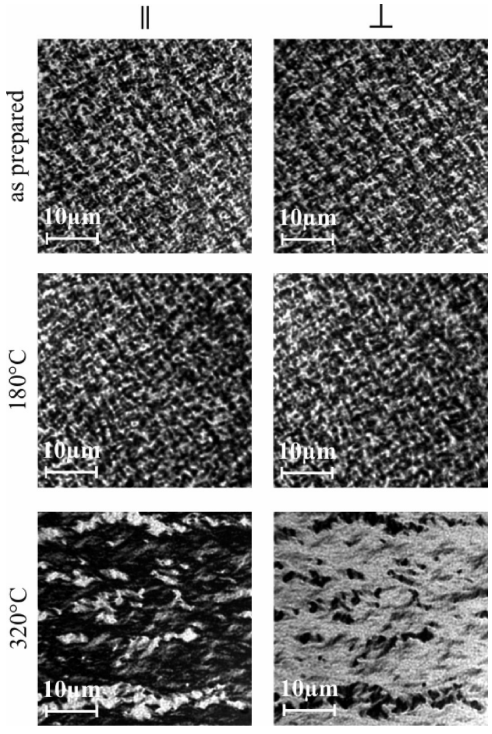

Figure 6. Polarized optical transmission of an as-prepared (top), annealed (middle), and melt-annealed film (bottom) at two polarization orientations.

are ~2 times lower than those measured in saturation, and the S-shaped output characteristics (Supporting Information Figure S1) are evidence of significant contact resistance.[38] Hence, the carrier mobility in the semiconductor might be even higher than the reported TFT mobility. By measuring the temperature dependence of the mobility, an Arrhenius relation is found, and the activation energy measured at V_d = 10 V is determined in the range of 100−240 K. When the sample is annealed at 150 °C, E_a = 60 meV, and after the melt treatment E_a = 63 meV, suggesting little change in activation energy as well. It should be noted that grazing incidence scattering measurements were performed on devices after testing to confirm that these films had undergone the same microstructural changes described above (Supporting Information Figure S1c,f). The similarity in mobility, threshold voltage, and activation energy for the devices based on the pre- and postmelt-annealed films therefore suggests one of two possible origins for this behavior. The first is that the large morphological change observed herein is not present at the interface. For example, the melt-annealed film shows a highly oriented fraction of crystallites at the buried interface (Figure 2c); it is possible that the 150 °C film also exhibits some edge-on character at the buried interface—perhaps just a monolayer—which would not be observed in the diffraction from the bulk film. The second possibility is that the texture change is present at the interface but that for this polymer the morphology and texture of the crystalline regions do not have a strong impact on the transistor performance. It could be that a large fraction of the interface is amorphous. This would be consistent with recent NEXAFS spectroscopy studies where it is reported that there exists a relatively large disordered content for both the conjugated core and side chains at both interfaces (with the buried interface exhibiting slightly better order than the top surface).[21] Alternatively, it is likely that the crystallite regions are not the transport bottlenecks in these TFTs. The high molecular weight used and the crystalline domain size suggest extensive intergrain sharing of a single polymer chain, enabling efficient transport pathways between grains.[19] However, it should be noted that even though the disordered regions may be the dominating factor for transistor transport, the crystallinity still plays a critical role in the high performance. Schuettfort et al. show that films annealed to the melt and quenched have an amorphous microstructure (by GIXD)[21] and have a marked drop in mobility (60−80%) compared to those annealed to 110 °C. This contrasts with our slowly cooled melt-annealed films where there is still high mobility (nearly the same as films annealed at 150 °C) and an increased crystallinity and strong (100) lamellar texture.

While the bottom-gate transistor performance is unaffected when the semiconductor film is melted and then slowly cooled, a large difference in charge transport is found in the direction perpendicular to the substrate surface as measured by electron-only sandwich devices (Figure 7b). In general, we observed that the current density increases linearly with bias for small voltages, indicative of small leakage currents (see Supporting Information Figure S2). At higher bias, the current−voltage characteristics follow a power law $j \propto V^n$, with $n \approx 3$ for all devices tested here. We point out that electron-only devices with the polymer batch used in this study had larger currents and a larger exponent n compared to devices prepared with an earlier batch.[9] The Mott−Gurney law for trap-free space charge limited currents predicts n = 2. Deviations from the Mott−Gurney law have been attributed to a distribution of transport states,[39] the presence of traps,[40] or inefficient carrier injection.[41] These mechanisms differ by their distinguished dependence of the current on layer thickness and bias. Therefore, an unambiguous explanation of the observed power-law would require measurements on samples within a large range of thicknesses, which is beyond the

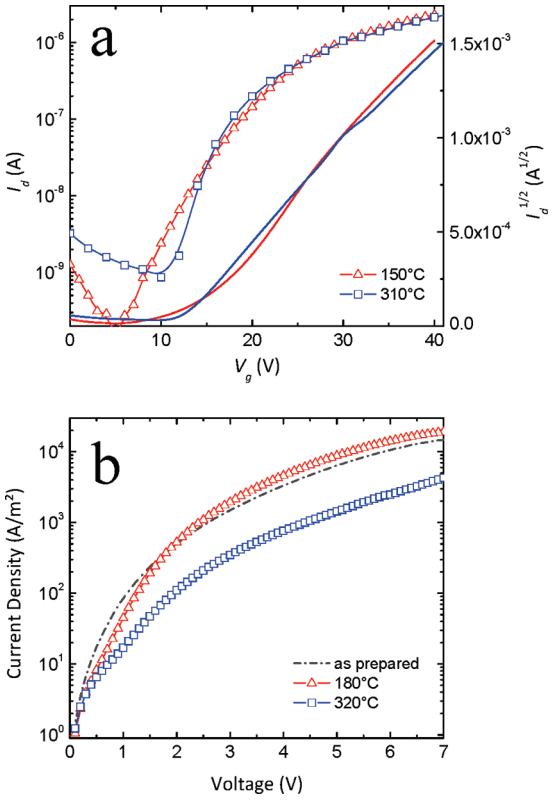

Figure 7. Device characterization for P(NDI2OD-T2) films annealed (red) and melt-annealed (blue). (a) Saturation regime transistor transfer characteristics showing little change in on current or mobility. (b) Electron currents perpendicular to the layer plane showing a significant drop in current density upon melt-annealing.

scope of the present paper. However, a qualitative comparison of the electron currents in different devices can be made, if the same layer thickness is chosen (meaning that the electric field in the layer at a given bias is the same for all devices), which is the case here.

In comparing the current density in the electron-only devices based on the as spun versus annealed (at 180 °C) P(NDI2OD-T2) films, a small current increase (~40%) is evident at 5−7 V. This can be due to the removal of residual solvent or minor reorientation effects. Upon melt annealing and slow cooling to ambient, there is a significant 6-fold reduction in current density (Figure 7b). These findings agree well with the morphological changes found by X-ray diffraction and polarized microscopy. Since our electron-only device measurements probe electron transport perpendicular to the semiconductor layer, there is a strong correlation between the electron-only current and the bulk film texture. The strong face-on texture in the 180 °C annealed film is found to yield high electron currents perpendicular to the substrate plane, in agreement with previous work.[9] The reduced current density observed for melt-annealed-based electron-only devices, despite the increased film crystallinity and intracrystalline order, highlights the importance of texture for transport through the bulk of this material.

CONCLUSIONS

This work investigates the striking texture change associated with annealing a film of P(NDI2OD-T2) to the melt and cooling to ambient at a slow rate. We used a variety of grazing incidence and specular diffraction techniques to describe the film morphological changes as well as in-situ diffraction to show that polymer chain reorientation occurs from the melt. We supplement this general finding with quantitative X-ray analysis in the form of complete pole figures and peak shape analysis. Pole figures quantitatively confirm the texture change from ~77% face-on crystallites to 94.5% edge-on and a 2-fold increase in crystallinity. The initial, largely face-on texture is likely due to kinetic trapping of the high molecular weight polymer chains during the spin-coating process. The melt anneal then moves the polymer toward thermodynamic equilibrium, which is the edge-on orientation. Warren−Averbach analysis reveals that both films have approximately the same crystallite sizes but that the paracrystalline disorder in the lamellar stacking direction in the crystallites of the melt-anneal film is reduced from 6.1% to 3.8%. The morphological changes are further explored using AFM and polarized microscopy. The implications for charge transport are obtained using bottom-gate TFT measurements and electron-only measurements. TFT saturation mobility exceeding 0.1 $cm^2/(V\ s)$ is found both before and after melt-annealing the semiconductor, suggesting that the morphological changes are either not present at the interface or not the limiting factor for in-plane charge transport. In contrast, a 6-fold reduction in bulk current density is observed for electron-only devices, confirming the importance of crystalline texture for electron transport perpendicular to the layer plane. This further suggests that while texture in P(NDI2OD-T2) may play a less important role for in-plane transistor transport in this material, it is of great relevance for applications where bulk transport is crucial, i.e., for diodes or photovoltaic charge collection. Although the crystalline portion of the film is certainly not the only factor relevant to transport, we have shown that diffraction and the quantitative techniques explored herein as well as the melt-anneal process are powerful tools to establish structure−property relations for semiconducting polymers.

ASSOCIATED CONTENT

Supporting Information. Figures S1 and S2 and Table S1. This material is available free of charge via the Internet at http://pubs.acs.org.

ACKNOWLEDGMENT

Portions of this research were carried out at the Stanford Synchrotron Radiation Lightsource, a national user facility operated by Stanford University on behalf of the U.S. Department of Energy, Office of Basic Energy Sciences. A.S. and J.R. gratefully acknowledge financial support from the National Science Foundation in the form of respectively a Career Award and a Graduate Student Fellowship. A.C. gratefully acknowledges funding from Amber Capital Investment Management received through the Italian Scientists and Scholars of North America Foundation. This publication was partially based on work supported by the Center for Advanced Molecular Photovoltaics (Award No. KUS-C1-015-21), made by King Abdullah University of Science and Technology (KAUST). The work in Potsdam was financially supported by the German Federal Ministry of Science and Education (BMBF FKZ 03X3525D). We thank Dr. Eric Verploegen for use of the in-situ heating chamber at SSRL beamline 11-3 and Dr. Stefan Mannsfeld for providing the 2D GIXS analysis software WxDiff. Polyera Corp.

thanks the FexTech Alliance for supporting the synthesis of P(NDI2OD-T2).

REFERENCES

(1) Klauk, H. *Organic Electronics: Materials, Manufacturing and Applications*; Wiley-VCH: Weinheim, Germany, 2006.

(2) Arias, A. C.; MacKenzie, J. D.; McCulloch, I.; Rivnay, J.; Salleo, A. *Chem. Rev.* **2010**, *110* (1), 3–24.

(3) Fabiano, S.; Chen, Z.; Vahedi, S.; Facchetti, A.; Pignataro, B.; Loi, M. A. *J. Mater. Chem.*

(4) Kim, J. B.; Lee, S.; Toney, M. F.; Chen, Z.; Facchetti, A.; Kim, Y. S.; Loo, Y.-L. *Chem. Mater.* **2010**, *22* (17), 4931–4938.

(5) de Leeuw, D. M.; Cantatore, E. *Mater. Sci. Semicond. Process.* **2008**, *11* (5−6), 199–204.

(6) Baeg, K.-J.; Khim, D.; Kim, D.-Y.; Jung, S.-W.; Koo, J. B.; You, I.K.; Yan, H.; Facchetti, A.; Noh, Y.-Y. *J. Polym. Sci., Part B: Polym. Phys.* **2010**, *49* (1), 62–67.

(7) Chen, Z.; Zheng, Y.; Yan, H.; Facchetti, A. *J. Am. Chem. Soc.* **2008**, *131* (1), 8–9.

(8) Yan, H.; Chen, Z.; Zheng, Y.; Newman, C.; Quinn, J. R.; Dotz, F.; Kastler, M.; Facchetti, A. *Nature* **2009**, *457* (7230), 679–686.

(9) Steyrleuthner, R.; Schubert, M.; Jaiser, F.; Blakesley, J. C.; Chen, Z.; Facchetti, A.; Neher, D. *Adv. Mater.* **2010**.

(10) Kline, R. J.; McGehee, M. D.; Kadnikova, E. N.; Liu, J.; Fréchet, J. M. J. *Adv. Mater.* **2003**, *15* (18), 1519–1522.

(11) Sirringhaus, H.; Brown, P. J.; Friend, R. H.; Nielsen, M. M.; Bechgaard, K.; Langeveld-Voss, B. M. W.; Spiering, A. J. H.; Janssen, R. A. J.; Meijer, E. W.; Herwig, P.; de Leeuw, D. M. *Nature* **1999**, *401* (6754), 685–688.

(12) DeLongchamp, D. M.; Vogel, B. M.; Jung, Y.; Gurau, M. C.; Richter, C. A.; Kirillov, O. A.; Obrzut, J.; Fischer, D. A.; Sambasivan, S.; Richter, L. J.; Lin, E. K. *Chem. Mater.* **2005**, *17* (23), 5610–5612.

(13) Zen, A.; Pflaum, J.; Hirschmann, S.; Zhuang, W.; Jaiser, F.; Asawapirom, U.; Rabe, J. P.; Scherf, U.; Neher, D. *Adv. Funct. Mater.* **2004**, *14* (8), 757–764.

(14) DeLongchamp, D. M.; Kline, R. J.; Lin, E. K.; Fischer, D. A.; Richter, L. J.; Lucas, L. A.; Heeney, M.; McCulloch, I.; Northrup, J. E. *Adv. Mater.* **2007**, *19* (6), 833–837.

(15) Hamadani, B. H.; Gundlach, D. J.; McCulloch, I.; Heeney, M. *Appl. Phys. Lett.* **2007**, *91* (24), 243512.

(16) Kline, R. J.; DeLongchamp, D. M.; Fischer, D. A.; Lin, E. K.; Heeney, M.; McCulloch, I.; Toney, M. F. *Appl. Phys. Lett.* **2007**, *90* (6), 062117.

(17) Kline, R. J.; DeLongchamp, D. M.; Fischer, D. A.; Lin, E. K.; Richter, L. J.; Chabinyc, M. L.; Toney, M. F.; Heeney, M.; McCulloch, I. *Macromolecules* **2007**, *40* (22), 7960–7965.

(18) McCulloch, I.; Heeney, M.; Bailey, C.; Genevicius, K.; MacDonald, I.; Shkunov, M.; Sparrowe, D.; Tierney, S.; Wagner, R.; Zhang, W.; Chabinyc, M. L.; Kline, R. J.; McGehee, M. D.; Toney, M. F. *Nature Mater.* **2006**, *5* (4), 328–333.

(19) Rivnay, J.; Toney, M. F.; Zheng, Y.; Kauvar, I. V.; Chen, Z.; Wagner, V.; Facchetti, A.; Salleo, A. *Adv. Mater.* **2010**, *22* (39), 4359–4363.

(20) Zhang, W.; Smith, J.; Watkins, S. E.; Gysel, R.; McGehee, M.; Salleo, A.; Kirkpatrick, J.; Ashraf, S.; Anthopoulos, T.; Heeney, M.; McCulloch, I. *J. Am. Chem. Soc.* **2010**, *132* (33), 11437–11439.

(21) Schuettfort, T.; Huettner, S.; Lilliu, S.; Macdonald, J. E.; Thomsen, L.; McNeill, C. R. *Macromolecules* **2011**, *44* (6), 1530–1539.

(22) Verploegen, E.; Mondal, R.; Bettinger, C. J.; Sok, S.; Toney, M. F.; Bao, Z. *Adv. Funct. Mater.* **2010**, *20* (20), 3519–3529.

(23) WxDiff is a diffraction image processing and data analysis software developed by Dr. S. C. B. Mannsfeld (SSRL); it is availible free of charge at http://code.google.com/p/wxdiff/.

(24) Baker, J. L.; Jimison, L. H.; Mannsfeld, S. C. B.; Volkman, S.; Yin, S.; Submramanian, V.; Salleo, A.; Alivisatos, A. P.; Toney, M. F. *Langmuir* **2010**, *26* (11), 9146–9151.

(25) Kline, R. J.; McGehee, M. D.; Toney, M. F. *Nature Mater.* **2006**, *5* (3), 222–228.

(26) Jimison, L. H. Understanding microstructure and charge transport in semi crystalline polythiophenes. Ph.D. Thesis, Stanford University, Stanford, CA, 2011.

(27) Crist, B.; Cohen, J. B. *J. Polym. Sci., Polym. Phys. Ed.* **1979**, *17* (6), 1001–1010.

(28) Warren, B. E.; Averbach, B. L. *J. Appl. Phys.* **1950**, *21* (6), 595–599.

(29) Rivnay, J.; Noriega, R.; Kline, R. J.; Salleo, A.; Toney, M. F. *Phys. Rev. B*, in press.

(30) Rivnay, J.; Noriega, R.; Northrup, J. E.; Kline, R. J.; Toney, M. F.; Salleo, A. *Phys. Rev. B* **2011**, *83*, 121306(R).

(31) Hindeleh, A. M.; Hosemann, R. *J. Phys. C: Solid State Phys.* **1988**, *21* (23), 4155.

(32) Hindeleh, A. M.; Hosemann, R. *J. Mater. Sci.* **1991**, *26* (19), 5127–5133.

(33) Prosa, T. J.; Moulton, J.; Heeger, A. J.; Winokur, M. J. *Macromolecules* **1999**, *32* (12), 4000–4009.

(34) Horowitz, G. *Adv. Mater.* **1998**, *10* (5), 365–377.

(35) Dimitrakopoulos, C. D.; Malenfant, P. R. L. *Adv. Mater.* **2002**, *14* (2), 99–117.

(36) Steyrleuthner, R.; Bange, S.; Neher, D. *J. Appl. Phys.* **2009**, *105* (6), 064509.

(37) Jimison, L. H.; Toney, M. F.; McCulloch, I.; Heeney, M.; Salleo, A. *Adv. Mater.* **2009**, *21*, 1568–1572.

(38) Caironi, M.; Newman, C.; Moore, J. R.; Natali, D.; Yan, H.; Facchetti, A.; Sirringhaus, H. *Appl. Phys. Lett.* **2010**, *96* (18), 183303.

(39) Pasveer, W. F.; Cottaar, J.; Tanase, C.; Coehoorn, R.; Bobbert, P. A.; Blom, P. W. M.; denbspLeeuw, D. M.; Michels, M. A. *J. Phys. Rev. Lett.* **2005**, *94* (20), 206601.

(40) Mark, P.; Helfrich, W. *J. Appl. Phys.* **1962**, *33* (1), 205–215.

(41) Emtage, P. R.; O'Dwyer, J. *J. Phys. Rev. Lett.* **1966**, *16* (9), 356.